Nano Research

Open Access

Research Article

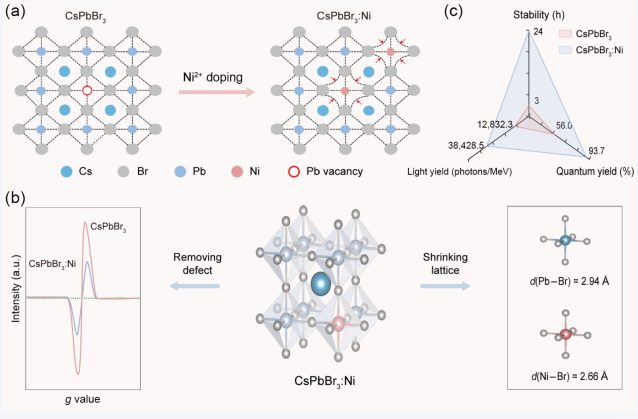
Engineering lattice and defects of nanosized metal halide perovskite via nickel doping for efficient X-ray imaging

Rufeng Wang[1], Yangmin Tang[2], Chenglong Qiu[1], Junnan Song[1], Zhenjie Cheng[1], Wei Chen[3], Yanxian Jin[1] ✉, Guiqiang Pu[1] ✉, and Jiacheng Wang[1] ✉

[1] *Zhejiang Key Laboratory for Island Green Energy and New Materials, Institute of Electrochemistry, School of Materials Science and Engineering, Taizhou University, Taizhou 318000, China*
[2] *Electronic Engineering Department, The Chinese University of Hong Kong, Hong Kong 999077, China*
[3] *Department of Materials Design and Innovation, University at Buffalo, The State University of New York, Buffalo, NY 14260, USA*

Cite this article: *Nano Research*, **2026**, *19*, 94908817. https://doi.org/10.26599/NR.2026.94908817

ABSTRACT: Metal halide perovskites (e.g., $CsPbBr_3$) have emerged as highly promising scintillator materials owing to their superior optoelectronic characteristics. However, their practical deployment is constrained by intrinsic structural instability and nonradiative recombination-induced energy loss. Herein, we show that Ni^{2+} doping constitutes a potent regulatory strategy for synergistically improving the scintillation performance and environmental robustness of $CsPbBr_3$ perovskite. Various characterizations combined with threotecial calculation indicate that the incorporation of Ni^{2+} dopants triggers lattice contraction, thereby enhancing the resistance to environmental perturbations. Ni-doping also passivates intrinsic defects and traps, leading to marked suppression of nonradiative recombination pathways. This synergy in as-prepared Ni-doped $CsPbBr_3$ leads to an 11-fold enhancement in photoluminescence intensity and a substantial increase in photoluminescence quantum yield from 56.0% to 93.7%. Notably, it delivers an exceptional light yield of 38,428.5 photons/MeV, a low detection limit of 64.9 nGy_{air}/s, and superior radiation tolerance. Furthermore, a flexible scintillation screen containing Ni-doped $CsPbBr_3$ enables high-resolution X-ray imaging with a spatial resolution of 16.6 lp/mm, notably surpassing that of the majority of reported perovskite-based scintillators. This study provides profound insights into the pivotal role of metal doping into halide perovskites for enhancing environmental stability in radiation detection technologies.



KEYWORDS: scintillator, metal halide perovskite, nickel doping engineering, environmental stability, X-ray imaging

1 Introduction

Scintillators convert high-energy ionizing radiation such as X-rays into visible light, serving applications in security screening, industrial inspection, scientific research, and medical diagnostics [1–5]. Superior stability, high light yield, and low detection limits are essential for achieving high-resolution X-ray imaging [6]. Currently, most commercial X-ray scintillators are inorganic compounds like bismuth germanate (BGO) and CsI:Tl, which exhibit outstanding X-ray scintillation properties, but generally suffer from shortcomings such as harsh fabrication conditions, high costs, and sensitivity to humidity and oxygen [7–14]. Novel X-ray scintillators (e.g., plastic and glass scintillators) have emerged as cost-effective alternatives to inorganic scintillation crystals [15–17]. Nevertheless, their low light yield (LY) and poor thermal stability impede practical deployment, rendering the development of high-efficiency and highly X-ray-sensitive scintillators with superior imaging resolution a critical challenge.

In recent years, metal halide perovskites have attracted considerable interest as a promising alternative class of scintillator materials [18–21]. All inorganic perovskite halides of cesium lead ($CsPbX_3$, where X = Cl, Br, or I) exhibit numerous advantages,

Received: March 18, 2026; **Revised:** April 27, 2026
Accepted: May 7, 2026

✉Address correspondence to Jiacheng Wang, jiacheng.wang@tzc.edu.cn; Guiqiang Pu, puguiqiang@tzc.edu.cn; Yanxian Jin, shirleyj@tzc.edu.cn

including low-cost fabrication, high effective atomic number, and outstanding optoelectronic performance. However, the insufficient environmental stability and low LY of $CsPbX_3$ stand as major bottlenecks impeding its practical deployment [22–25]. For instance, $CsPbI_3$ possesses the appropriate bandgap for efficient luminescence, but its native form exhibits severe phase instability at room temperature. It readily transforms from the light-active black phase to a non-perovskite yellow phase, causing a drastic decline in scintillation capability [26]. $CsPbCl_3$ is renowned for its high-energy luminescence spanning the ultraviolet to violet regions, a property highly valuable for specific detection applications. It often exhibits low photoluminescence quantum yield (PLQY) due to strong phonon scattering and deep-level defects [27]. Moreover, even emerging lead-free alternatives such as $CsCu_2I_3$, which have garnered significant attention for their exceptional environmental stability and low toxicity, typically exhibit limited LY and suffer from low PLQY. These limitations constrain their performance in practical imaging applications [28]. In short, the commercialization of $CsPbX_3$ scintillators still faces considerable challenges.

The existing transition metal dopants (such as Mn^{2+} and Zn^{2+}) are usually introduced to optimize a single property. For instance, Cai et al. were able to adjust the distortion of $[Cu_2I_5]^{3-}$ in the ground state/excited state by doping Zn into the Cu1 site, significantly enhancing the luminescence efficiency of $Cs_3Cu_2I_5$ [29]. Gong et al. incorporated manganese ions into Cs_2ScCl_5. Mn^{2+} arranged in octahedral structures separated by scandium ions could more effectively suppress photogenerated carriers, which was beneficial for improving the PLQY [30]. However, Mn^{2+} doping introduces more luminescent centers and generates a luminescence phenomenon with a longer lifetime, which leads to the appearance of different post-luminescence blurred images and is not conducive to X-ray imaging. Herein, we propose that Ni^{2+} doping engineering is an effective strategy to simultaneously improve the stability, PLQY, and LY of $CsPbBr_3$ scintillator (Figs. 1(a) and 1(c)). On the one hand, Ni^{2+} doping can maintain the intrinsic nanosecond-level rapid flicker attenuation of $CsPbBr_3$. This rapid response characteristic reduces the afterglow effect, avoids image blurring during continuous imaging, and ensures the clarity of rapid imaging. Electron paramagnetic resonance (EPR) and in-depth spectroscopy analysis reveal that the introduction of Ni^{2+} can passivate harmful lead vacancies of $CsPbBr_3$, thereby suppressing carrier trapping at these defect sites, promoting radiative recombination, and achieving near-unity PLQY (left in Fig. 1(b)). On the other hand, density functional theory (DFT) calculations combined with stability analysis confirm that Ni^{2+} doping effectively induces lattice contraction in $CsPbBr_3$, leading to the formation of Ni–Br bonds that possess higher stability than the intrinsic Pb–Br bonds (right in Fig. 1(b)), thereby better resisting the structural degradation caused by radiation. As a result, the modified crystal structure maintains outstanding stability against ultraviolet irradiation and humid ambient conditions. Benefiting from the aforementioned modifications, Ni-doped $CsPbBr_3$ ($CsPbBr_3$:Ni) exhibits excellent scintillation performance including a high LY of 38,428.5 photons/MeV and a detection limit as low as 64.9 nGy_{air}/s, along with excellent radiation and environmental stability (Fig. 1(c)). Moreover, the high resolution of an optimized flexible scintillator screen prepared by mixing polydimethylsiloxane (PDMS) with $CsPbBr_3$:Ni could reach up to 16.6 lp/mm, holding a promise for practical X-ray imaging.

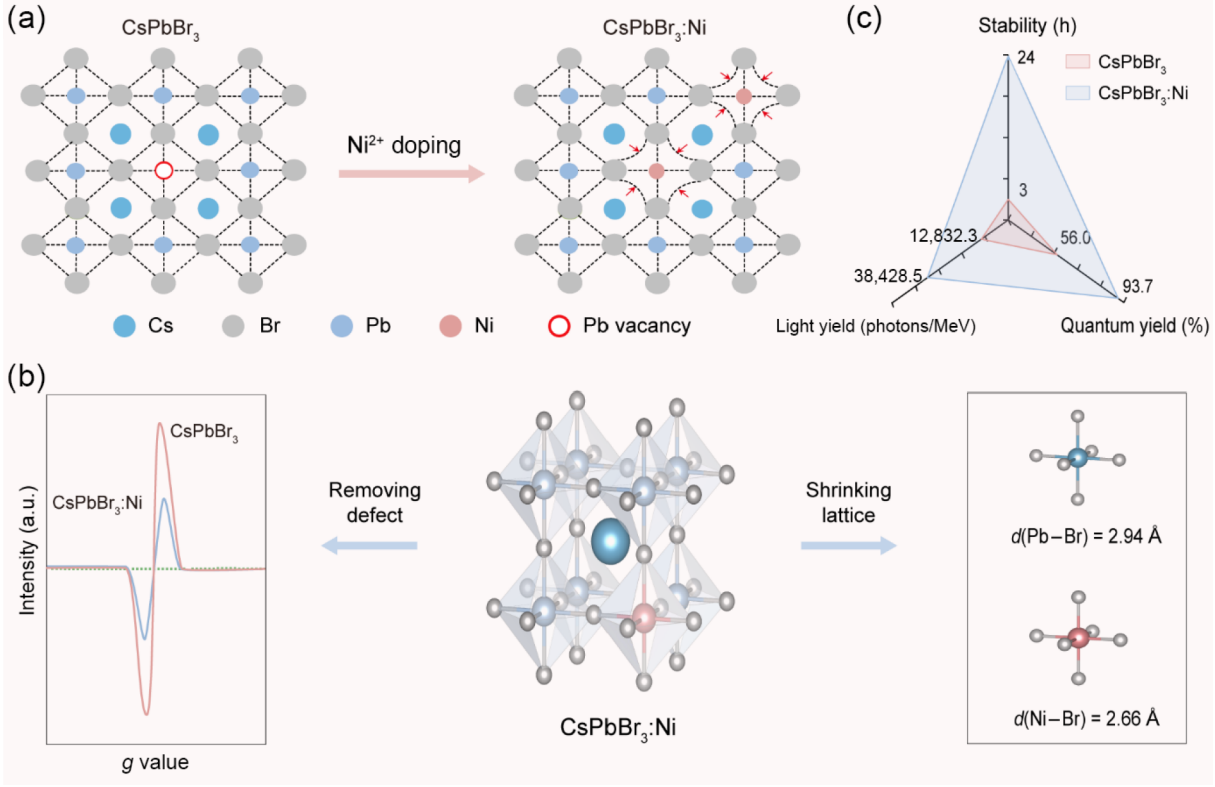


Figure 1 (a) Schematic illustration of the introduction of Ni^{2+} into the lattice of $CsPbBr_3$, effectively suppressing vacancy formation. (b) The effect of Ni^{2+} doping on defects and lattice in $CsPbBr_3$. The Ni^{2+} doping could remove the defects and shrink the lattice. (c) The satellite map of PLQY, LY, stability for both $CsPbBr_3$ and $CsPbBr_3$:Ni.

2 Experimental

2.1 Chemicals

Cesium carbonate (Cs_2CO_3, 99.9%), oleic acid (OA, 90%), 1-octadecene (ODE, 90%), lead(II) bromide ($PbBr_2$, 99.99%), $NiBr_2$, oleylamine (OAm, C18-content 80%–90%), and cyclohexane (≥ 99.7%) were purchased from Shanghai Aladdin Biochemical Technology Co., Ltd. All reagents were used as received without further purification.

2.2 Synthesis of $CsPbBr_3$ nanocrystals

In a typical synthesis procedure, Cs_2CO_3 (0.05 g), OA (0.35 mL), and ODE (5 mL) were added to a two-neck round-bottom flask (100 mL). Next, the resulting mixture was heated at 110 °C under vigorous stirring and vacuum conditions for 1 h. After that, a nitrogen purge and vacuum were alternately applied to the flask three times to remove moisture and O_2. Subsequently, the reaction temperature was maintained at 120 °C under N_2 atmosphere and stirred until all Cs_2CO_3 reacted with OA to form Cs-oleate. A clear solution was obtained. Notably, Cs-oleate precipitated in the ODE at ambient temperature and had to be preheated to 100 °C before it could be used for the subsequent synthesis of perovskite nanocrystal.

The $CsPbBr_3$ perovskite nanocrystals were synthesized by a modified hot-injection procedure [31]. In a typical experiment, $PbBr_2$ (0.188 mol) and 5 mL of ODE were added to a two-neck round-bottom flask (100 mL). Next, the resulting mixture was heated at 110 °C under vigorous stirring and vacuum conditions for 1 h, at which time the moisture residue was removed by purging with nitrogen and vacuum suction. Then, OA (0.5 mL) and OAm (0.5 mL) preheated to 70 °C was injected into the flask under N_2. The flask was heated at 120 °C until $PbBr_2$ completely reacted with OA and OAm. Then, the mixture was heated to 180 °C until the $PbBr_2$ precursors dissolved completely. A hot Cs-oleate precursor solution (0.8 mL) was injected quickly into the above reaction mixture. After 5 s of reaction, the flask was transferred into an ice. The as-prepared $CsPbBr_3$ crude solutions were precipitated by centrifuging at 8000 rpm for 10 min. The colored supernatant was carefully discarded, and the precipitate was mixed with cyclohexane (6 mL) using an ultrasonic cleaner. The solution was centrifuged at 8000 rpm in 10 min. Then, the perovskite nanocrystals were dispersed in cyclohexane (6 mL) and centrifuged at 12,000 rpm for 5 min to remove any excess Cs-oleate, larger perovskite nanocrystals, and agglomerates. Finally, after repeating the previous step once, the precipitate was then collected and redispersed in cyclohexane, resulting in a colloidal dispersion of the $CsPbBr_3$.

2.3 Synthesis of Ni-doped $CsPbBr_3$ nanocrystals

The synthesis of the Ni-doped $CsPbBr_3$ ($CsPbBr_3$:Ni) nanocrystals was performed in a manner similar to that of the $CsPbBr_3$ nanocrystals, as described above. ODE (5 mL), $PbBr_2$, and $NiBr_2$ were added to a two-necked round-bottom flask (100 mL) and dried under vacuum at 110 °C for 1 h. All other experimental operations, including precursor injection, reaction temperature control, and post-synthesis purification, were maintained consistent with the standard procedure for pristine $CsPbBr_3$ nanocrystals.

2.4 Device fabrication

PDMS and scintillator powder were mixed in a mass ratio of 10:1 and stirred to form a uniform mixture of gel. The mixture was then evenly scraped onto a PET film. The mold was heated at 60 °C and held for 10 h.

2.5 Material characterizations

X-ray powder diffraction (XRD, Bruker D8 Advance) was used to analyze the phase structure of the powder. Microstructure was observed using transmission electron microscopy (TEM, Thermo Fisher Scientific Talos F200i). The valence state of the powder was determined using X-ray photoelectron spectroscopy (XPS, Shimadzu AXIS Supra+). The absorption spectra were obtained using a ultraviolet–visible (UV–vis) spectrophotometer (MAPADA, UV-670). Photoluminescence (PL) excitation and emission spectra were measured using a fluorescence spectrophotometer (Techcomp, FL970 Plus) with an excitation wavelength of 375 nm. Time-resolved PL spectra were measured by using a spectrofluorometer (Edinburgh Instruments, FLS1000). All temperature variation measurements were performed with an additional device. X-ray imaging measurements were carried out using a home-built system consisting of an X-ray source, a scintillator film, and a digital camera. The radiation dose of X-rays was controlled by changing the current and voltage of the X-ray source. By adjustment of the voltage and current of the X-ray source, the radiation dose could be regulated. The operational voltage and current of the X-ray source ranged from 0 to 50 kV and from 0 to 80 μA, respectively. In the X-ray imaging process, the sample was placed between the scintillator screen and the X-ray source. A camera was utilized to capture images from the other side of the scintillator film. To protect the camera from X-ray damage, a reflector was also utilized. Specifically, the distance between the X-ray source and the scintillator screen was 12 cm. The scintillator screen and the reflector were separated by 15 cm, while the distance from the reflector to the camera was 30 cm. The object to be imaged was placed in direct contact with the scintillator to minimize image blurring. All imaging experiments were performed under an X-ray source operating at 50 kV and 35 μA, with a dose of 278 μGy_{air}/s and an exposure time of 8 s.

2.6 Computational and sim

DFT calculations were performed using the Vienna *ab initio* simulation package (VASP) [32], employing the generalized gradient approximation (GGA) with the Perdew–Burke–Ernzerhof (PBE) exchange-correlation functional [33, 34]. A plane-waveenergy cutoff of 450 eV and a 3 × 3 × 3 Monkhorst–Pack grid for *k*-point sampling were set to ensure numerical precision. Convergence criteria were established at 10^{-5} eV for energy and 0.02 eV/Å for forces. To analyze the bonding properties, the wave functions obtained by VASP were projected using local orbital basissuite towards electronic-structure reconstruction (LOBSTER) toobtain the crystal orbital Hamilton population (COHP) [35]. Andthe integrated projected crystal orbital Hamilton population (IpCOHP) was obtained by integrating the energy-resolved COHPcurves from the band bottom up to the Fermi level.

3 Results and discussion

3.1 Structural characterizations of Ni-doped $CsPbBr_3$

$CsPbBr_3$:*x*Ni (*x* = 0%, 1.25%, 2.5%, 3.75%, and 5%) nanocrystals were synthesized via the hot-injection method (Fig. S1 in the

Electronic Supplementary Material (ESM)). The specific synthesis steps are available in the ESM. The TEM images show that all samples exhibit a similar cubic morphology, while the average particle size of the samples gradually decreases from 18 to 14 nm with the increase of Ni^{2+} doping concentration from 0% to 5% (Figs. 2(a) and 2(b), and Fig. S2 in the ESM) [36]. XRD analysis confirms the phase purity of $CsPbBr_3$:*x*Ni, with all diffraction patterns corresponding to the orthorhombic phase of $CsPbBr_3$ (PDF #18-0364, left in Fig. 2(c)). It is noteworthy that the diffraction peaks slightly shift to higher angles with increasing Ni^{2+} doping concentration, indicating the occurrence of lattice contraction (right in Fig. 2(c)). This observation is consistent with the successful substitution of Pb^{2+} by Ni^{2+}, given the smaller ionic radius (r = 0.69 Å) of Ni^{2+} ions compared to that of Pb^{2+} ions (r = 1.19 Å) [37]. Figure 2(d) demonstrates the high crystallinity of $CsPbBr_3$ before and after Ni^{2+} doping, and the fast Fourier transform pattern confirms their distinct lattice fringes. Notably, the lattice spacing of $CsPbBr_3$ decreased from 0.407 to 0.401 nm compared to $CsPbBr_3$:2.5Ni, which further confirms the lattice contraction induced by Ni^{2+} doping [38]. Moreover, energy dispersive X-ray spectroscopy (EDS) mapping images reveal that the elements Cs, Pb, Br, and Ni are evenly distributed into the whole nanoparticles, which demonstrates the successful doping of Ni^{2+} into the lattice (Fig. 2(e)).

XPS of $CsPbBr_3$:2.5Ni was performed to further evaluate the bonding state of doped Ni^{2+} within the lattice. The full scan spectrum of $CsPbBr_3$:2.5Ni reveals the existence of Ni 2p-related peak in addition to the intrinsic Cs, Pb, and Br elements (Fig. S3 in the ESM). Furthermore, a comparison of the high-resolution Pb 4f spectra between $CsPbBr_3$ and $CsPbBr_3$:2.5Ni shows a slight increase in binding energy for $CsPbBr_3$:2.5Ni (Fig. 2(f)). A similar shift toward higher binding energy (0.3 eV) is observed for the Br 3d peaks (Fig. 2(g)). This indicates a modified chemical environment after the Ni^{2+} combination. Furthermore, the actual concentrations of Ni^{2+} and Pb^{2+} were determined by inductively coupled plasma-optical emission spectroscopy (ICP-OES). The molar ratio of Ni:Pb was tested to be 1.8%, as is shown in Table S1 in the ESM, slightly lower than the feeding molar ratio. Based on the above experimental results, it can be confirmed that Ni^{2+} has been doped into the $CsPbBr_3$ lattice by substituting Pb^{2+} sites or vacancies.

3.2 Regulation of the photophysical properties of $CsPbBr_3$ by Ni^{2+} doping

Following the successful synthesis, we then proceeded to investigate the influence of Ni^{2+} doping on the photophysical properties of $CsPbBr_3$. Figure 3(a) presents the absorption spectra of $CsPbBr_3$:*x*Ni. The results indicate that the absorption edge lies within the wavelength range of 512–518 nm (Table S2 in the ESM).

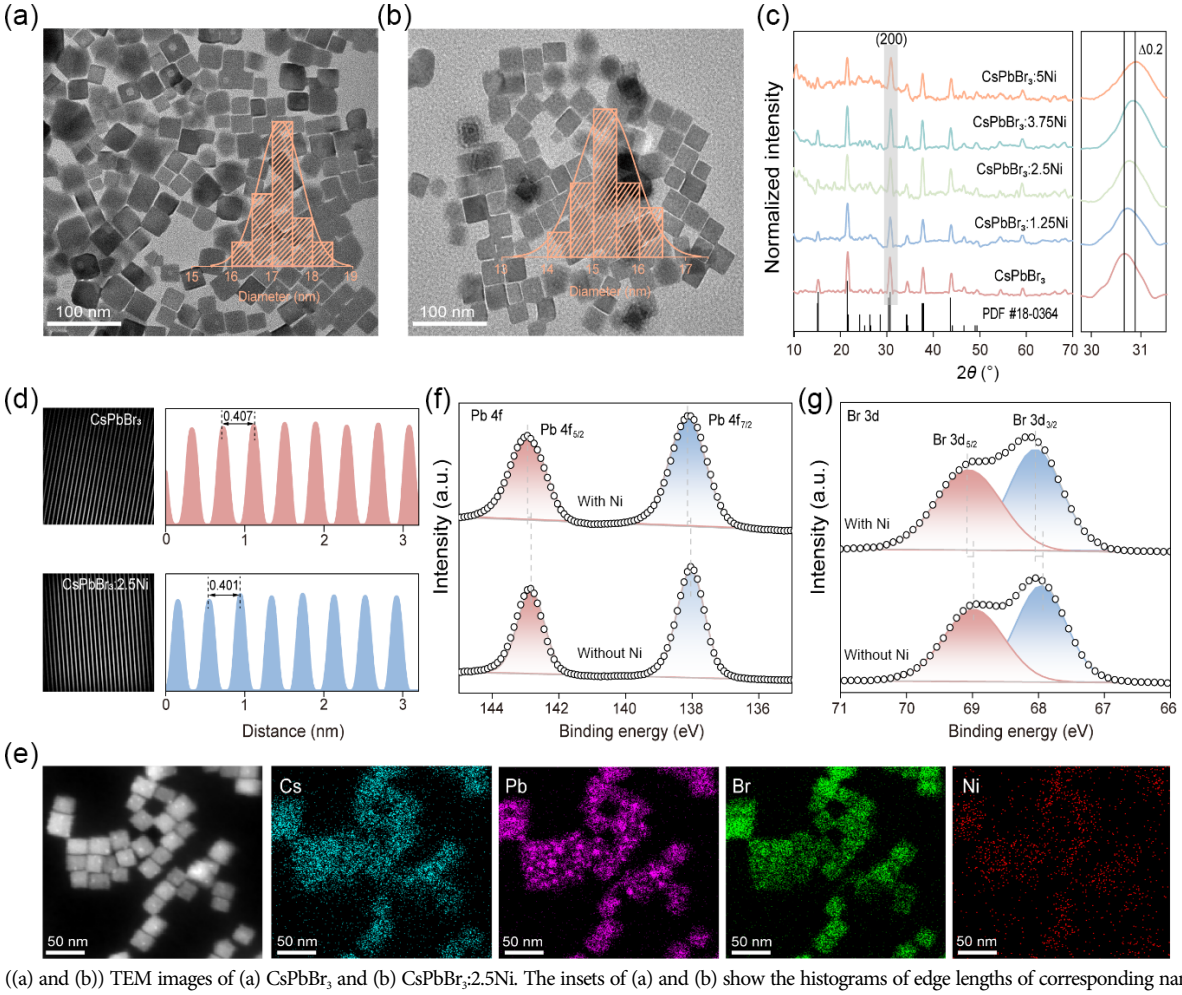


Figure 2 ((a) and (b)) TEM images of (a) $CsPbBr_3$ and (b) $CsPbBr_3$:2.5Ni. The insets of (a) and (b) show the histograms of edge lengths of corresponding nanocrystals. (c) XRD patterns of $CsPbBr_3$ doped with Ni at different concentrations. (d) Measured values of the atomic distance and intensity profile of $CsPbBr_3$ and $CsPbBr_3$:2.5Ni. (e) Elemental mapping images of $CsPbBr_3$:2.5Ni. ((f) and (g)) High-resolution XPS spectra of (f) Pb 4f and (g) Br 3d.

It is attributed to the introduction of Ni^{2+}-induced shallow states near the valence band maximum, as revealed by our DFT analysis. It is noteworthy that Ni^{2+} doping resulted in a negligible effect on the absorption of $CsPbBr_3$. Figure 3(b) shows the PL spectra of $CsPbBr_3$:*x*Ni. With increasing Ni^{2+} doping concentration, the PL emission peak exhibits a systematic blue shift from 531 to 518 nm. This shift indicates that Ni^{2+} doping effectively passivates defects in the $CsPbBr_3$ [39, 40]. Meanwhile, the PL intensity initially increases with increasing Ni^{2+} doping concentration and then reaches a maximum at 2.5% Ni^{2+} doping. However, as the Ni^{2+} doping concentration continues to increase, the PL intensity decreases as a result of concentration quenching [41]. As shown in Fig. 3(c) and Fig. S4 in the ESM, the PLQY increases sharply from 56.0% to 93.7% at an Ni^{2+} doping concentration of 2.5%, indicating that nonradiative recombination phenomena in $CsPbBr_3$:2.5Ni are negligible. The significant increase in PLQY suggests that intrinsic defect passivation is the underlying mechanism.

To verify the above hypothesis, we then performed the EPR spectroscopy measurements (Fig. 3(d)). Both $CsPbBr_3$ and $CsPbBr_3$:2.5Ni exhibit a resonance signal at $g \approx 2.005$, which is characteristic of unpaired electrons associated with charge-compensating defects [42]. Notably, the intensity of this characteristic EPR signal is significantly diminished in $CsPbBr_3$:2.5Ni. This suppression also strongly evidences that Ni^{2+}

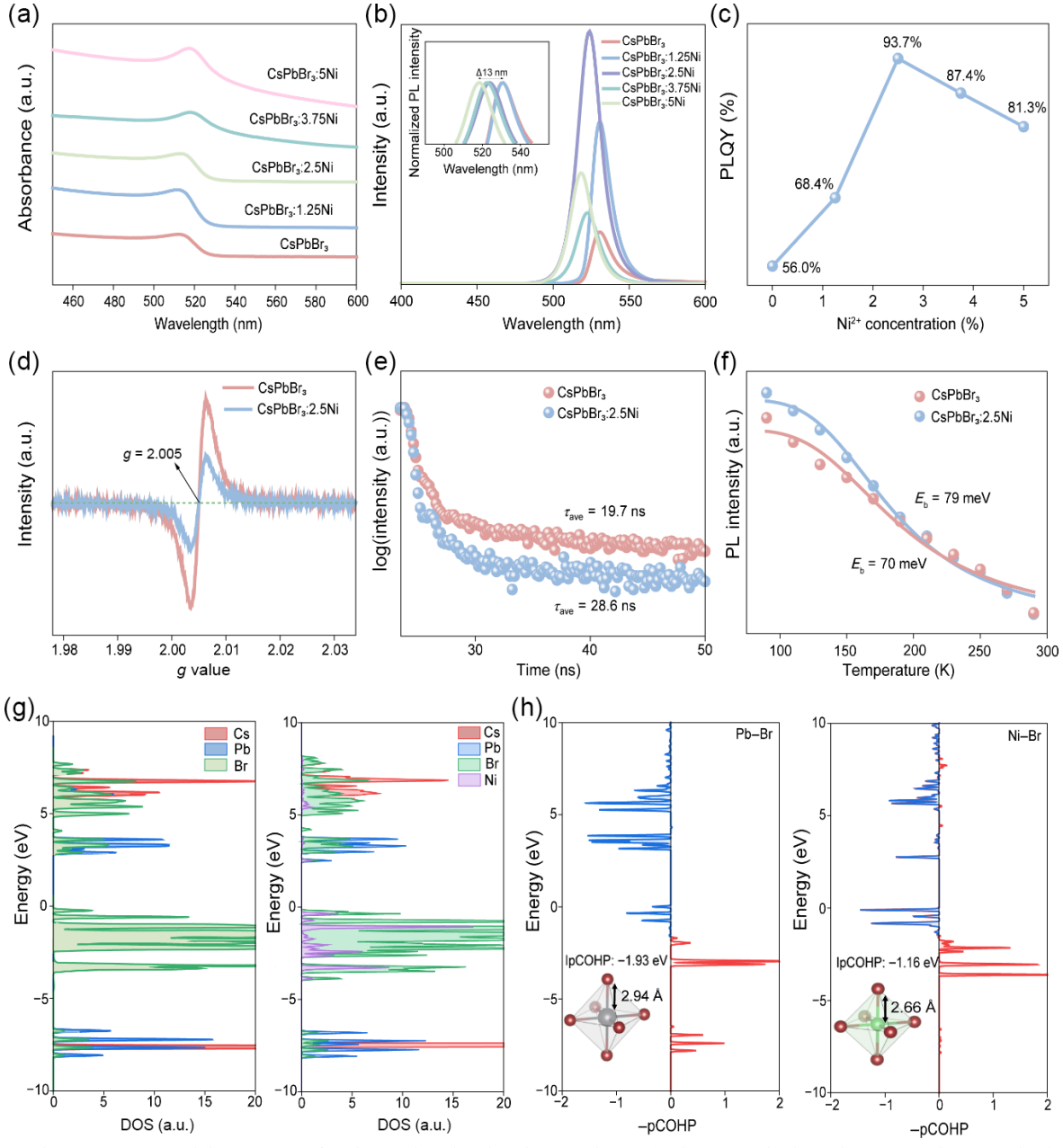


Figure 3 (a) Absorption spectra and (b) PL spectra of $CsPbBr_3$ and Ni-doped $CsPbBr_3$ ($CsPbBr_3$:*x*Ni). The inset in (b) shows the corresponding normalized PL spectra. (c) PLQYs of $CsPbBr_3$:*x*Ni (*x* = 0, 1.25, 2.5, 3.75, and 5). (d) EPR of $CsPbBr_3$ and $CsPbBr_3$:2.5Ni. (e) Time-resolved PL decay of $CsPbBr_3$ and $CsPbBr_3$:2.5Ni. (f) Temperature-dependent curves of the corresponding PL integral intensities for $CsPbBr_3$ and $CsPbBr_3$:2.5Ni. ((g) and (h)) Density of states (DOS) and pCOHP plots for Pb–Br and Ni–Br interactions in (g) $CsPbBr_3$ and (h) $CsPbBr_3$:Ni, respectively. The integral of COHP to the Fermi level (IpCOHP) has been shown to better quantify the outcome of interatomic interactions. The energy axis is referenced to the Fermi level.

doping effectively passivates related defects. Consequently, this effective defect passivation channels more excited carriers through radiative recombination pathways, enabling the $CsPbBr_3$:2.5Ni to achieve a PLQY approaching nearly 100%. The time-resolved kinetic measurements show a marked extension of the decay lifetime from 19.7 to 28.6 ns upon Ni^{2+} doping into $CsPbBr_3$ (Fig. 3(e)). Moreover, the radiative and nonradiative decay rates can also be calculated using the PLQY and the average lifetimes (Table S3 in the ESM) [36, 43]. The radiative decay rate increased slightly from 0.0284 to 0.0328 ns^{-1} after the introduction of Ni^{2+} ions. In stark contrast, the nonradiative decay rate was drastically suppressed, decreasing from 0.0223 to 0.0022 ns^{-1}. Therefore, the enhanced optical properties of $CsPbBr_3$ are primarily attributed to Ni^{2+} ions doping, which effectively suppresses non-radiative recombination by passivating defects.

Then, we performed DFT calculation to understand the origin of Ni^{2+} doping induced photophysical properties of $CsPbBr_3$. First, the bandgap was analyzed using the Tauc plot method. Notably, the bandgap decreased slightly from 2.38 eV for $CsPbBr_3$ to 2.36 eV for $CsPbBr_3$:Ni (Fig. S5 in the ESM). As illustrated in Figs. S6 and S7 in the ESM, both the valence band maximum (VBM) and the conduction band minimum (CBM) of $CsPbBr_3$ and $CsPbBr_3$:Ni are located at the Γ point. The calculated bandgap for the $CsPbBr_3$ is approximately 1.67 eV, which is lower than the experimental value, a common underestimation in standard DFT calculations [44]. For the $CsPbBr_3$:Ni, the calculated bandgap is reduced to 1.12 eV, aligning with the Tauc plot analysis trend. The main contributions to the conduction band (CB) and the valence band (VB) are provided by Pb atoms and Br atoms, respectively (left in Fig. 3(g)). The Cs atoms have no significant contribution. As shown in Fig. 3(g)(right), the band gap of $CsPbBr_3$:Ni is almost unchanged with respect to $CsPbBr_3$ and a localized energy state associated with Ni dopants near the VBM appears. Notably, it should be mentioned that the band-edge emission of $CsPbBr_3$ is of excitonic nature, which is mainly due to the recombination of the excited electron with self-trapped hole [45]. Moreover, the Ni^{2+}-induced shallow states provide a favorable pathway for hole capture, which effectively suppresses nonradiative recombination at defect and thereby enhances the radiative decay rate and PLQY. These findings offer direct evidence for the proposed defect passivation mechanism.

We then measured the temperature-dependent PL spectra to further investigate the influence of Ni^{2+} doping on the photophysical properties of $CsPbBr_3$ (Figs. S8 and S9 in the ESM). Both samples show a gradual decrease in PL intensity with increasing temperature, which is attributed to thermally activated nonradiative recombination. The overall temperature-dependent PL intensity can be described by Eq. (1) [46, 47]

$$I(T) = \frac{I_0}{1 + Ae^{-E_b/k_B T}} \quad (1)$$

where $I(T)$ and I_0 represent the PL intensities at temperatures T and 0 K, respectively; A, k_B, and E_b denote the constant, Boltzmann constant, and exciton binding energy, respectively. As shown in Fig. 3(f), the exciton binding energy of the $CsPbBr_3$:2.5Ni is 79 meV, higher than that of the $CsPbBr_3$ (70 meV). The larger E_b enhances the stability of excitons at room temperature (where thermal energy is 26 meV) and even higher temperatures, thereby improving the thermal stability of $CsPbBr_3$ through Ni^{2+} ions doping. Furthermore, the full width at half-maximum (FWHM) broadens with increasing temperature (Figs. S10 and S11 in the ESM), a phenomenon precisely fitted by employing a Bose–Einstein model accounting for exciton–phonon interactions during the carrier recombination [46, 47].

$$\Gamma(T) = \Gamma_0 + \sigma T + \frac{\Gamma_{OP}}{e^{\hbar\omega_{op}/k_B T} - 1} \quad (2)$$

The Γ_0, σT, and $\Gamma_{OP}/e^{\hbar\omega op/kBT}-1$ in the mode correspond to non-uniform broadening, exciton–phonon, and exciton–phonon interactions, respectively. The symbol $\hbar\omega_{op}$ represents the optical phonon energy. The fitting results indicate that the optical phonon energies of both samples are similar, with values of 18.92 meV for $CsPbBr_3$ and 19.37 meV for $CsPbBr_3$:2.5Ni. These nearly identical values indicate that Ni^{2+} doping does not significantly alter the lattice vibrational properties of the host material.

3.3 The effects of Ni^{2+} doping on the environmental stabitliy of $CsPbBr_3$

In further experiments, we subsequently investigated the effect of Ni^{2+} doping on the ambient stabistality to $CsPbBr_3$ (Fig. S12(a) in the ESM). The photostability of the samples was rigorously tested under continuous irradiation using a portable 3 W ultraviolet lamp as the light source (irradiance: 350 μW/cm^2). The PL intensity of the $CsPbBr_3$ abruptly decreased to 45.1% of its initial value after 24 h (Fig. S13(a) in the ESM), indicating that the inherent susceptibility of pristine materials to light-induced damage. In contrast, the $CsPbBr_3$:2.5Ni demonstrated exceptional robustness, retaining 81.5% of its initial PL intensity under the same conditions (Fig. S13(b) in the ESM). The PL intensity decay in the $CsPbBr_3$:2.5Ni was significantly reduced, demonstrating the substantial enhancement in photodegradation resistance conferred by Ni^{2+} doping.

In addition, the humid stability of metal halide perovskites is a critical factor for their practical applications. To evaluate this property, water stability tests were conducted on $CsPbBr_3$ and $CsPbBr_3$:2.5Ni by adding deionized water (5% by volume) to the colloidal solution. To enable direct and effective comparison, we simultaneously performed time-dependent PL measurements on solutions of the same concentration of $CsPbBr_3$ and $CsPbBr_3$:2.5Ni. The PL intensity evolution curves reveal a significant difference in stability (Fig. S12(b) in the ESM). $CsPbBr_3$ undergoes rapid hydrolysis degradation, exhibiting substantial intensity decay within the first minute of water exposure. As shown in Fig. S13(c) in the ESM, it indicates rapid aggregation and structural disintegration of the nanocrystals upon water intrusion. In stark contrast, $CsPbBr_3$:2.5Ni exhibited exceptional stability. Its PL spectrum remains largely unchanged over time, and the fluorescence quenching kinetics are markedly slowed, with the material retaining over 78% of its initial PL intensity after prolonged testing (Fig. S13(d) in the ESM). Consequently, this significantly enhanced water stability demonstrates that Ni^{2+} doping effectively mitigates the inherent susceptibility of $CsPbBr_3$ to hydrolysis, representing a key breakthrough for its application in ambient or humid environments.

The impact of Ni^{2+} doping on structural stability of $CsPbBr_3$ was further elucidated through bonding analysis. As previously discussed, Ni^{2+} ions replaced Pb^{2+} sites in the $CsPbBr_3$ lattice. This substitution replaces partial Pb–Br bonds with Ni–Br bonds, reducing the bond length from 2.94 to 2.66 Å and resulting in significant lattice contraction. The further calculation of pCOHP

demonstrates that the Ni–Br bond is more stable than the Pb–Br bond by approximately 0.77 eV (Fig. 3(h)), as evidenced by their integrated pCOHP values of −1.93 and −1.16 eV. This enhanced bonding character contributes to improved lattice stability. These results confirm that the lattice contraction from Ni^{2+} ions doping yields a more compact and stable crystal structure, thereby enhancing the stability of $CsPbBr_3$.

3.4 Investigation of the scintillation properties of $CsPbBr_3$:2.5Ni

The excellent PL stability and high PLQY (~ 94%) make $CsPbBr_3$:2.5Ni a promising candidate for X-ray scintillators. To demonstrate its scintillation performance, we compared the X-ray absorption spectra of $CsPbBr_3$ and $CsPbBr_3$:2.5Ni with those of several commercial scintillators (e.g., Si and LYSO:Ce) in Fig. 4(a). Notably, the X-ray absorbance of $CsPbBr_3$:2.5Ni is much superior to that of silicon and approaches that of LYSO:Ce, demonstrating excellent X-ray absorption capacity. The LY, a key performance metric, reflects the efficiency of the scintillator in converting high-energy radiation into visible light [48]. The LY of $CsPbBr_3$:2.5Ni was determined as high as 38,428.5 photons/MeV, using the commercial BGO scintillator with a known LY (9000 photons/MeV) as a reference (Fig. 4(b)). This value is far superior to that of pristine $CsPbBr_3$ and the commercial BGO. Besides the high LY, the practical utility of a scintillator also depends on its response characteristics under varying irradiation conditions.

Figure 4(c) shows that the radioluminescence (RL) intensity of $CsPbBr_3$:2.5Ni demonstrates a significant increase with an increased dose rate (DL) from 12.5 to 278 $\mu Gy_{air}/s$, and the RL intensity and dose rate show a large range linear correlation, suggesting a stable light output under X-ray radiation. The X-ray detection limit can be calculated to be 64.9 nGy_{air}/s, which is less than one-sixteenth of the dose rate used in traditional X-ray medical diagnostics (5500 nGy_{air}/s) [49]. In addition, irradiation stability is also a critical indicator related to safety requirements and lifespan. After intermittent exposure to a high X-ray dose for 1800 s, the RL intensity of $CsPbBr_3$:2.5Ni barely changed (Fig. 4(d))). Figure S14 in the ESM shows the RL intensity measured after exposure to X-ray irradiation lasting from 30 s to 10 min. $CsPbBr_3$ shows a relatively low irradiation stability, and the RL intensity significantly decreases to 90% after 10 min of irradiation. The integral RL intensity of $CsPbBr_3$:2.5Ni retains 97% of its initial value after 10 min of irradiation. All results indicate that $CsPbBr_3$:2.5Ni can offer excellent scintillation performance for long periods. There is no doubt that both the enhanced LY and the radiation stability of $CsPbBr_3$ stem from effective Ni^{2+} doping engineering.

Based on the above experimental results, we proposed a plausible radioluminescence and X-ray stability mechanism for Ni^{2+} doped $CsPbBr_3$ scintillator. As shown in Fig. 4(e), under X-ray irradiation, the scintillator absorbs high-energy photons primarily via the photoelectric effect and Compton scattering, generating numerous primary electrons and holes. This initiates a cascade of charge carrier dynamics: These high-energy electrons ionize other atoms along their trajectories through Coulomb interactions, producing secondary high-energy electrons. The resulting thermal carriers subsequently undergo thermalization, cooling down to the band

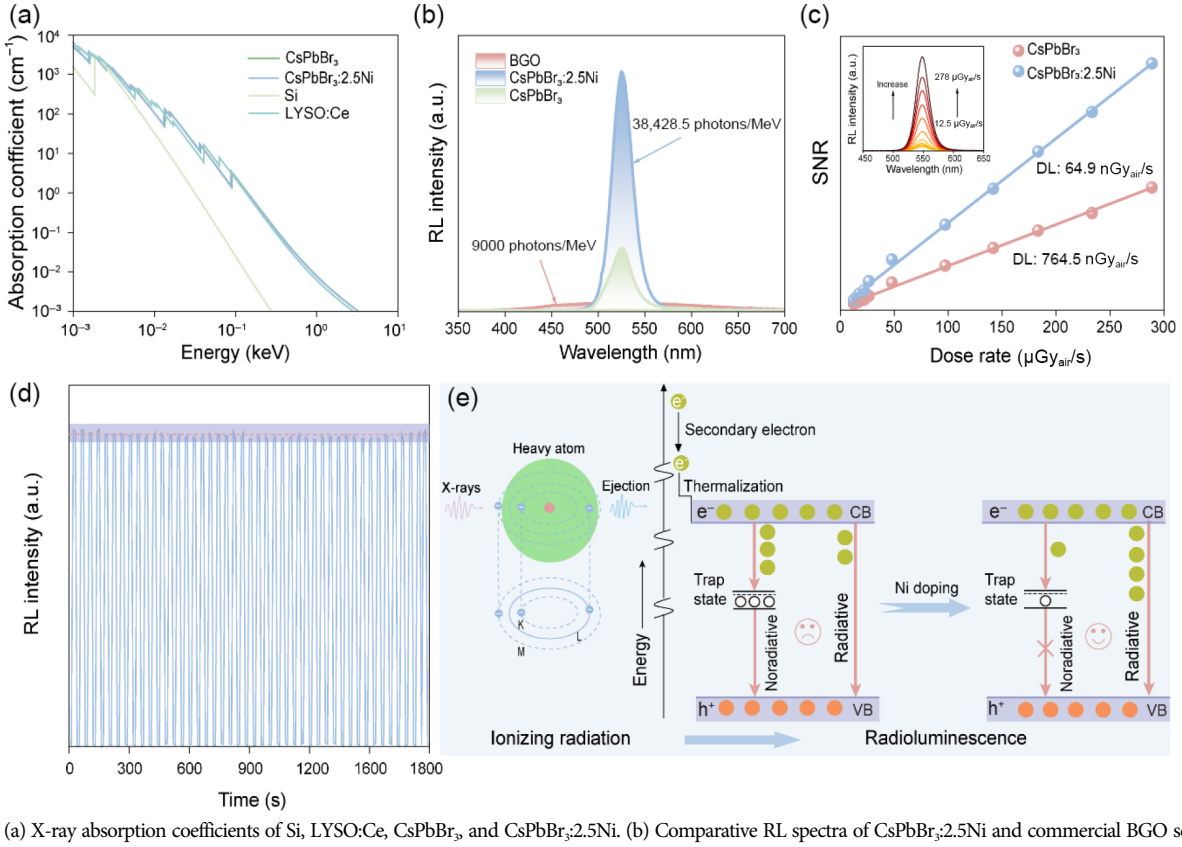


Figure 4 (a) X-ray absorption coefficients of Si, LYSO:Ce, $CsPbBr_3$, and $CsPbBr_3$:2.5Ni. (b) Comparative RL spectra of $CsPbBr_3$:2.5Ni and commercial BGO scintillator. (c) The dependence of the RL intensity of $CsPbBr_3$ and $CsPbBr_3$:2.5Ni on the dose rate, exhibiting a linear relationship. The Pearson's correlation coefficients (r) of all of the fitted results were greater than 0.99. The inset shows the RL spectra of $CsPbBr_3$:2.5Ni under X-ray irradiation at different dose rates. (d) Radiation stability of $CsPbBr_3$:2.5Ni under continuous X-ray irradiation. (e) Schematic diagram of the scintillation mechanism of $CsPbBr_3$:2.5Ni.

edges. In $CsPbBr_3$, a significant fraction of these thermalized carriers is trapped by intrinsic lattice defects. At these defect sites, carriers predominantly recombine through non-radiative pathways, whereby the recombination energy is dissipated as heat into the lattice via multi-phonon emission instead of being converted into light. This process directly diminishes the light output of the scintillator. The Ni^{2+} doping engineering has jointly enhanced the X-ray stability and radiation luminescence. On the one hand, Ni^{2+} doping effectively induces lattice contraction in $CsPbBr_3$, leading to the formation of Ni–Br bonds that possess higher stability than the intrinsic Pb–Br bonds. This makes it more difficult for structural degradation and ion migration under the thermal effect and ionization generated by high-energy X-ray irradiation. On the other hand, Ni^{2+} doping engineered effectively passivates these intrinsic defects, thereby suppressing non-radiative recombination channels. This optimization of carrier recombination pathway directs more carriers toward radiative recombination centers, resulting in the release of their energy as photons and thus producing highly efficient radioluminescence. Consequently, the synergistic effects of Ni^{2+} doping engineering deliver both highly efficient radioluminescence and exceptional stability.

3.5 Application of Ni-doped $CsPbBr_3$ scintillator in X-ray imaging

$CsPbBr_3$:2.5Ni has the integrated merits of strong X-ray absorption, high LY, and long-term operational stability, which are necessary for achieving high-performance X-ray imaging. Benefiting from the flexibility and optical transparency of PDMS, $CsPbBr_3$:2.5Ni can be homogeneously dispersed in the PDMS matrix to fabricate a scintillator film. The detailed preparation procedures of these flexible films are illustrated in Section 2. A custom-built system was applied to conduct an X-ray imaging experiment (Fig. 5(a)). The object was placed between the X-ray source and the scintillator screen, and the resulting image was captured with a digital camera. Figure 5(b) presents the RL spectra of $CsPbBr_3$:2.5Ni scintillation film. The inset shows its bright green emission under X-ray excitation, which is notably more intense than the emission from the $CsPbBr_3$ scintillation film. According to the slanted-edge method, the imaging spatial resolution of $CsPbBr_3$:2.5Ni scintillator can be described by the modulation transfer function (MTF). At MTF = 0.2, the scintillation film based on $CsPbBr_3$:2.5Ni exhibited an X-ray imaging resolution of 15.5 lp/mm, significantly surpassing the 10.9 lp/mm of $CsPbBr_3$ (Fig. 5(c)). The imaging resolution is far superior to that of commercial CsI:Tl (3 to 5 lp/mm) [50]. The enhanced X-ray imaging capability of $CsPbBr_3$:2.5Ni arises from increase in light yield and radiative recombination rate.

Furthermore, we photographed an X-ray standard line pair card and the results show that the observable limit of the line pair is 16.6 lp/mm, which echoes the results by using the slanted-edge method (Fig. 5(d)). The distribution curves of relative gray value of these scintillation screens (Fig. 5(e)) are extracted from Fig. 5(d) and Fig. S15 in the ESM. The corresponding relative gray-scale distribution curves further validate the exceptional spatial resolution of the $CsPbBr_3$:2.5Ni scintillator film. As shown in Fig. 5(f), an encapsulated metallic spring and an electronic chip are clearly

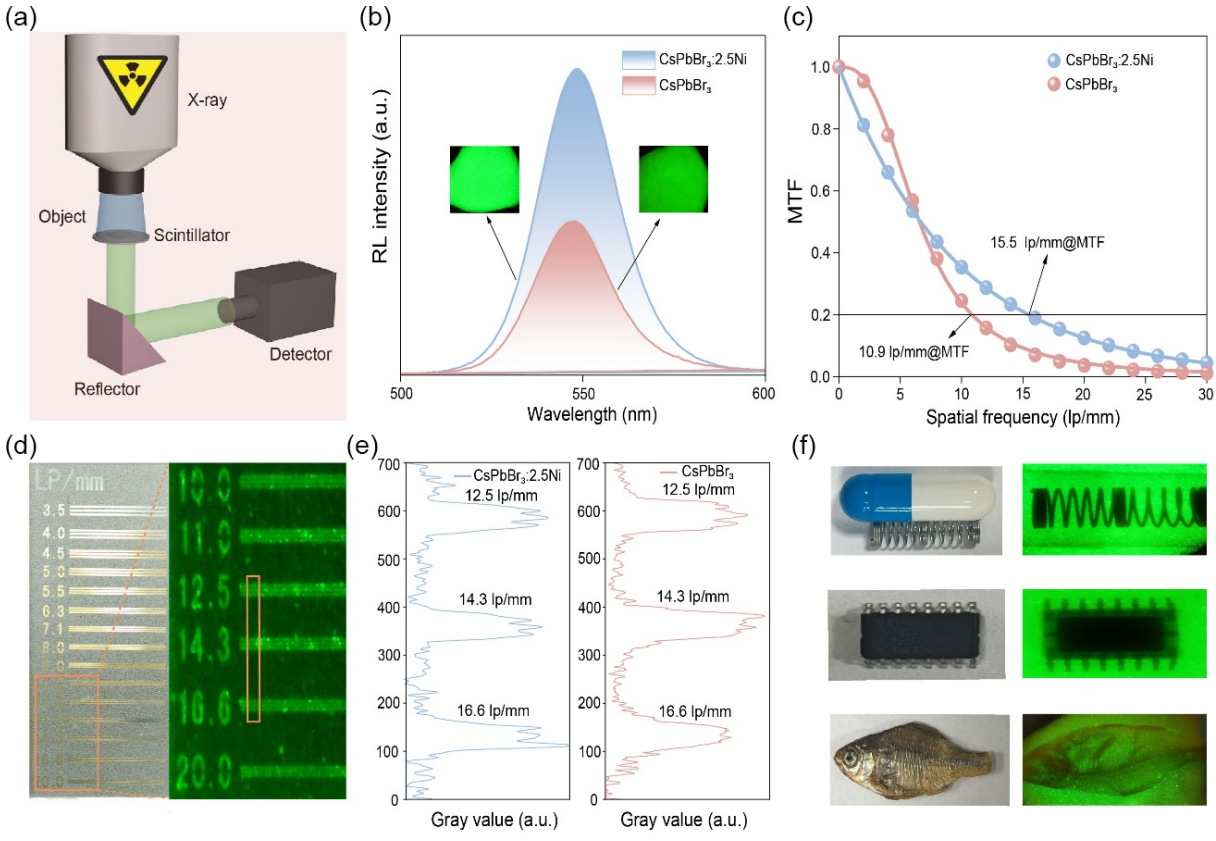


Figure 5 (a) Schematic diagram of X-ray imaging device. (b) Comparative RL spectra of $CsPbBr_3$:2.5Ni and $CsPbBr_3$. The inset shows a luminescence photograph of the flexible scintillator screen. (c) MTF analysis of $CsPbBr_3$ and $CsPbBr_3$:2.5Ni based scintillation films. (d) Bright-field (left) and X-ray excitation (right) images of a standard X-ray resolution pattern plate (area ranging from 3.5 to 20 lp/mm) using $CsPbBr_3$:2.5Ni film scintillator. (e) Relative gray value distribution curves for $CsPbBr_3$ and $CsPbBr_3$:2.5Ni, ranging from 12.5 to 16.6 lp/mm. (f) The photographs and corresponding X-ray images of capsule, chip, and fish.

visualized, demonstrating their potential applications in security screening and industrial inspection. Additionally, the biological tissues within the fish body are distinctly resolved, highlighting their potential for medical imaging. These X-ray imaging demonstrations indicate that $CsPbBr_3$:2.5Ni scintillator shows great potential for practical application.

4 Conclusions

In summary, we successfully demonstrated that Ni^{2+} doping engineering is an effective strategy to significantly enhance the scintillation performance and environmental stability of $CsPbBr_3$. Introducing Ni^{2+} into the $CsPbBr_3$ lattice induces lattice contraction and effectively passivates intrinsic defects, thereby significantly suppressing nonradiative recombination pathways. This passivation effect leads to an 11-fold increase in PL intensity and an increase in PLQY from 56.0% to 93.7% while simultaneously prolonging the PL lifetime. As a scintillator, $CsPbBr_3$:2.5Ni exhibits an impressive LY of 38,428.5 photons/MeV, a low detection limit of 64.9 nGy_{air}/s, and excellent irradiation stability. Moreover, a $CsPbBr_3$:2.5Ni@PDMS flexible scintillator screen demonstrates great imaging ability, achieving a spatial resolution of 16.6 lp/mm. Our work not only demonstrates a high-performance and low-cost scintillation material, but also provides deep insights into the crucial role of metal ion doping in suppressing defects and optimizing perovskite scintillator performance.

Electronic Supplementary Material: Supplementary material (photograph of reaction solution, TEM images, XPS spectra, PLQYs, band structures, temperature-dependent PL spectra, PL stability testing, RL stability testing, ICP-OES, and radiative and non-radiative rate) is available in the online version of this article at https://doi.org/10.26599/NR.2026.94908817.

Data availability

All data needed to support the conclusions in the paper are presented in the manuscript and the Electronic Supplementary Material. Additional data related to this paper may be requested from the corresponding author upon request.

Acknowledgements

The authors are grateful for the financial support from the Central Guidance on Science and Technology Development Fund of Zhejiang Province (No. 2024ZY01011) and the National Natural Science Foundation of China (No. 22402144).

Declaration of competing interest

All the contributing authors report no conflict of interests in this work.

Author contribution statement

R. F. W. designed and engineered the samples. C. L. Q. performed the DFT simulation. Y. M. T. and J. N. S. performed the experiments. R. F. W. wrote the paper with support from Z. J. C., W. C., Y. X. J., G. Q. P., and J. C. W. All the authors have approved the final manuscript.

Use of AI statement

None.

References

[1] Wang, C. L.; Zhao, Y.; Ma, T. S.; An, Y. D.; He, R.; Zhu, J. W.; Chen, C.; Ren, S. Q.; Fu, F.; Zhao, D. W. et al. A universal close-space annealing strategy towards high-quality perovskite absorbers enabling efficient all-perovskite tandem solar cells. *Nat. Energy* **2022**, *7*, 744–753.

[2] Ou, X. Y.; Qin, X.; Huang, B. L.; Zan, J.; Wu, Q. X.; Hong, Z. Z.; Xie, L. L.; Bian, H. Y.; Yi, Z. G.; Chen, X. F. et al. High-resolution X-ray luminescence extension imaging. *Nature* **2021**, *590*, 410–415.

[3] Pu, G. Q.; Wang, R. F.; Tang, Y. M.; Song, J. N.; Wang, J. C. Cation doping engineering of metal halide perovskites for high-energy X-ray exploration. *Mater. Chem. Front.* **2025**, *9*, 1954–1970.

[4] Gan, N.; Zou, X.; Dong, M. Y.; Wang, Y. Z.; Wang, X.; Lv, A. Q.; Song, Z. C.; Zhang, Y. Y.; Gong, W. Q.; Zhao, Z. et al. Organic phosphorescent scintillation from copolymers by X-ray irradiation. *Nat. Commun.* **2022**, *13*, 3995.

[5] Deng, M. X.; Tang, Y. M.; Chen, J. F.; Tang, Y. F.; Wang, J.; Sun, T. M.; Wang, M. M.; Zhu, J. L.; Zhou, Z. Z.; Wang, J. C. Bismuth vacancy-induced Enhancement of luminescence intensity and irradiation resistance for $Bi_4Ge_3O_{12}$. *J. Phys. Chem. Lett.* **2023**, *14*, 3818–3825.

[6] Kakavelakis, G.; Gedda, M.; Panagiotopoulos, A.; Kymakis, E.; Anthopoulos, T. D.; Petridis, K. Metal halide perovskites for high-energy radiation detection. *Adv. Sci.* **2020**, *7*, 2002098.

[7] Zhou, Y.; Chen, J.; Bakr, O. M.; Mohammed, O. F. Metal halide perovskites for X-ray imaging scintillators and detectors. *ACS Energy Lett.* **2021**, *6*, 739–768.

[8] Zhang, Z. Z.; Wei, J. H.; Luo, J. B.; Wang, X. D.; He, Z. L.; Kuang, D. B. Large-area laminar TEA_2MnI_4 single-crystal scintillator for X-ray imaging with impressive high resolution. *ACS Appl. Mater. Interfaces* **2022**, *14*, 47913–47921.

[9] Yuan, J. W.; Peng, Q. C.; Fu, J. C.; Yang, Q.; Gao, Z. Y.; Wang, Z. Y.; Li, K.; Zang, S. Q.; Tang, B. Z. Highly efficient stable luminescent radical-based X-ray scintillator. *J. Am. Chem. Soc.* **2023**, *145*, 27095–27102.

[10] Liang, S.; Zhang, M. Y.; Biesold, G. M.; Choi, W.; He, Y. J.; Li, Z. L.; Shen, D. F.; Lin, Z. Q. Recent advances in synthesis, properties, and applications of metal halide perovskite nanocrystals/polymer nanocomposites. *Adv. Mater.* **2021**, *33*, 2005888.

[11] Jana, A.; Cho, S.; Patil, S. A.; Meena, A.; Jo, Y.; Sree, V. G.; Park, Y.; Kim, H.; Im, H.; Taylor, R. A. Perovskite: Scintillators, direct detectors, and X-ray imagers. *Mater. Today* **2022**, *55*, 110–136.

[12] Yao, Q.; Li, J. M.; Li, X. S.; Ma, Y. S.; Song, H. H.; Li, Z. Y.; Wang, Z. G.; Tao, X. T. Achieving a record scintillation performance by micro-doping a heterovalent magnetic ion in $Cs_3Cu_2I_5$ single-crystal. *Adv. Mater.* **2023**, *35*, 2304938.

[13] Liu, X. M.; Li, R. H.; Xu, X. L.; Jiang, Y. Y.; Zhu, W. J.; Yao, Y.; Li, F. Y.; Tao, X. F.; Liu, S. J.; Huang, W. et al. Lanthanide(III)-Cu_4I_4 organic framework scintillators sensitized by cluster-based antenna for high-resolution X-ray imaging. *Adv. Mater.* **2023**, *35*, 2206741.

[14] Xu, L. J.; Lin, X. S.; He, Q. Q.; Worku, M.; Ma, B. W. Highly efficient eco-friendly X-ray scintillators based on an organic manganese halide. *Nat. Commun.* **2020**, *11*, 4329.

[15] Zhao, C. H.; Wang, Y. Z.; Bao, S. Y.; Zang, Y. S.; Liu, X. W.; Huang, W. High-performance hybrid organic-inorganic lanthanide halide glass scintillators enabled by dehydration for efficient X-ray imaging. *Adv. Mater.* **2025**, *37*, 2500925.

[16] Son, J.; Kim, D. G.; Lee, S.; Park, J.; Kim, Y.; Schaarschmidt, T.; Kim, Y. K. Improved 3D printing plastic scintillator fabrication. *J. Korean Phys. Soc.* **2018**, *73*, 887–892.

[17] Min, S.; Kang, H.; Seo, B.; Roh, C.; Hong, S.; Cheong, J. Integrated

and portable probe based on functional plastic scintillator for detection of radioactive cesium. *Appl. Sci.* **2021**, *11*, 5210.
[18] Zhou, Y.; Chen, J.; Bakr, O. M.; Sun, H. T. Metal-doped lead halide perovskites: Synthesis, properties, and optoelectronic applications. *Chem. Mater.* **2018**, *30*, 6589–6613.
[19] Yun, R.; Yang, H. X.; Sun, W. D.; Zhang, L. B.; Liu, X. W.; Zhang, X. D.; Li, X. Y. Recent advances on Mn^{2+}-doping in diverse metal halide perovskites. *Laser Photonics Rev.* **2023**, *17*, 2200524.
[20] Kim, H.; Huynh, K. A.; Kim, S. Y.; Le, Q. V.; Jang, H. W. 2D and quasi-2D halide perovskites: Applications and progress. *Phys. Status Solidi RRL-Rapid Res. Lett.* **2020**, *14*, 1900435.
[21] Nguyen, V. H.; Do, H.; Van Nguyen, T.; Singh, P.; Raizada, P.; Sharma, A.; Sana, S.; Grace, A. N.; Shokouhimehr, M.; Ahn, S. H.; Xia, C. L. et al. Perovskite oxide-based photocatalysts for solar-driven hydrogen production: Progress and perspectives. *Sol. Energy* **2020**, *211*, 584–599.
[22] Wang, T.; Zeng, G. Q.; Yang, Y. M.; Yang, Z.; Wang, T. C.; Li, H.; Han, L. L.; Yu, X.; Xu, X. H.; Ouyang, X. P. Advances in metal halide perovskite scintillators for X-ray detection. *Nano-Micro Lett.* **2025**, *17*, 275.
[23] Tang, Y. M.; Pu, G. Q.; Liu, Q. N.; Li, J.; Wang, X. Z.; Suenaga, K.; Bi, H.; Chen, W.; Wang, J. C. Metal halide perovskite enriched with entropy-induced lattice distortion for enhanced X-ray detection. *ACS Nano* **2025**, *19*, 30396–30406.
[24] Lee, T. W. Emerging halide perovskite materials and devices for optoelectronics. *Adv. Mater.* **2019**, *31*, 1905077.
[25] Lee, D. E.; Kim, S. Y.; Jang, H. W. Lead-free all-inorganic halide perovskite quantum dots: Review and outlook. *J. Korean Ceram. Soc.* **2020**, *57*, 455–479.
[26] Dutta, A.; Pradhan, N. Phase-stable red-emitting $CsPbI_3$ nanocrystals: Successes and challenges. *ACS Energy Lett.* **2019**, *4*, 709–719.
[27] Gao, L.; Gong, Y. Y.; Zhang, X. Y.; Yip, H. L.; Shen, L.; Zhang, J. Q. Metal halide perovskites blue emitters and light-emitting diodes: A review on morphological and molecular dimensions. *Laser Photonics Rev.* **2024**, *18*, 2301100.
[28] Cheng, S. L.; Beitlerova, A.; Kucerkova, R.; Mihokova, E.; Nikl, M.; Zhou, Z. Y.; Ren, G. H.; Wu, Y. T. Non-hygroscopic, self-absorption free, and efficient 1D $CsCu_2I_3$ perovskite single crystal for radiation detection. *ACS Appl. Mater. Interfaces* **2021**, *13*, 12198–12202.
[29] Yang, Q. H.; Li, G. H.; Ao, Y. C.; Zhao, S. J.; Wei, H. Q.; Fu, L.; Luo, Z. W.; Zhou, T. L.; Wang, C. J.; Cai, G. M. Green massive mechanical synthesis of highly efficient Zn-doped $Cs_3Cu_2I_5$ for LED and X-ray imaging applications. *Chem. Eng. J.* **2024**, *500*, 157230.
[30] Cao, M. Y.; Li, R. F.; Li, Z. L.; Zhao, X. J.; Gong, X. Efficient red-emitting lead-free cesium-scandium halide perovskite crystals produced via Mn^{2+} doping. *Sci. China Mater.* **2024**, *67*, 1340–1347.
[31] Swarnkar, A.; Marshall, A. R.; Sanehira, E. M.; Chernomordik, B. D.; Moore, D. T.; Christians, J. A.; Chakrabarti, T.; Luther, J. M. Quantum dot-induced phase stabilization of α-$CsPbI_3$ perovskite for high-efficiency photovoltaics. *Science* **2016**, *354*, 92–95.
[32] Kresse, G.; Furthmüller, J. Efficient iterative schemes for *ab initio* total-energy calculations using a plane-wave basis set. *Phys. Rev. B* **1996**, *54*, 11169–11186.
[33] Blöchl, P. E. Projector augmented-wave method. *Phys. Rev. B* **1994**, *50*, 17953–17979.
[34] Perdew, J. P.; Burke, K.; Ernzerhof, M. Generalized gradient approximation made simple. *Phys. Rev. Lett.* **1996**, *77*, 3865–3868.
[35] Maintz, S.; Deringer, V. L.; Tchougréeff, A. L.; Dronskowski, R. LOBSTER: A tool to extract chemical bonding from plane-wave based DFT. *J. Comput. Chem.* **2016**, *37*, 1030–1035.
[36] Yong, Z. J.; Guo, S. Q.; Ma, J. P.; Zhang, J. Y.; Li, Z. Y.; Chen, Y. M.; Zhang, B. B.; Zhou, Y.; Shu, J.; Gu, J. L. et al. Doping-enhanced short-range order of perovskite nanocrystals for near-unity violet luminescence quantum yield. *J. Am. Chem. Soc.* **2018**, *140*, 9942–9951.
[37] Xing, K.; Yuan, X.; Wang, Y.; Li, J.; Wang, Y. J.; Fan, Y.; Yuan, L.; Li, K.; Wu, Z. J.; Li, H. B. et al. Improved doping and emission efficiencies of Mn-doped $CsPbCl_3$ perovskite nanocrystals via nickel chloride. *J. Phys. Chem. Lett.* **2019**, *10*, 4177–4184.
[38] Pan, G. C.; Bai, X.; Xu, W.; Chen, X.; Zhai, Y.; Zhu, J. Y.; Shao, H.; Ding, N.; Xu, L.; Dong, B. et al. Bright blue light emission of Ni^{2+} ion-doped $CsPbCl_xBr_{3-x}$ perovskite quantum dots enabling efficient light-emitting devices. *ACS Appl. Mater. Interfaces* **2020**, *12*, 14195–14202.
[39] Wang, X. B.; Liu, S. Y.; Wang, H. H.; Luo, J. S. Side chain functional molecule additives for efficient and stable perovskite solar cells. *Adv. Funct. Mater.* **2024**, *34*, 2403104.
[40] Shao, Y. C.; Xiao, Z. G.; Bi, C.; Yuan, Y. B.; Huang, J. S. Origin and elimination of photocurrent hysteresis by fullerene passivation in $CH_3NH_3PbI_3$ planar heterojunction solar cells. *Nat. Commun.* **2014**, *5*, 5784.
[41] Xu, H. P.; Liang, W. Q.; Zhang, Z. Z.; Cao, C.; Yang, W. S.; Zeng, H. M.; Lin, Z. E.; Zhao, D. W.; Zou, G. H. 2D perovskite Mn^{2+}-doped $Cs_2CdBr_2Cl_2$ scintillator for low-dose high-resolution X-ray imaging. *Adv. Mater.* **2023**, *35*, 2300136.
[42] Pi, J. C.; Jia, X. F.; Long, Z. W.; Yang, S.; Wu, H.; Zhou, D. C.; Wang, Q.; Zheng, H. B.; Yang, Y.; Zhang, J. Y. et al. Surface and defect engineering coupling of halide double perovskite $Cs_2NaBiCl_6$ for efficient CO_2 photoreduction. *Adv. Energy Mater.* **2022**, *12*, 2202074.
[43] Imran, M.; Caligiuri, V.; Wang, M. J.; Goldoni, L.; Prato, M.; Krahne, R.; De Trizio, L.; Manna, L. Benzoyl halides as alternative precursors for the colloidal synthesis of lead-based halide perovskite nanocrystals. *J. Am. Chem. Soc.* **2018**, *140*, 2656–2664.
[44] Eperon, G.; Stranks, S. D.; Menelaou, C.; Johnston, M. B.; Herz, L. M.; Snaith, H. J. Formamidinium lead trihalide: A broadly tunable perovskite for efficient planar heterojunction solar cells. *Energy Environ. Sci.* **2014**, *7*, 982–988.
[45] Brennan, M. C.; Herr, J. E.; Nguyen-Beck, T. S.; Zinna, J.; Draguta, S.; Rouvimov, S.; Parkhill, J.; Kuno, M. Origin of the size-dependent stokes shift in $CsPbBr_3$ perovskite nanocrystals. *J. Am. Chem. Soc.* **2017**, *139*, 12201–12208.
[46] Zhang, F.; Shi, Z. F.; Ma, Z. Z.; Li, Y.; Li, S.; Wu, D.; Xu, T. T.; Li, X. J.; Shan, C. X.; Du, G. T. Silica coating enhances the stability of inorganic perovskite nanocrystals for efficient and stable down-conversion in white light-emitting devices. *Nanoscale* **2018**, *10*, 20131–20139.
[47] Ma, Z. Z.; Shi, Z. F.; Yang, D. W.; Zhang, F.; Li, S.; Wang, L. T.; Wu, D.; Zhang, Y. T.; Na, G. R.; Zhang, L. J. et al. Electrically-driven violet light-emitting devices based on highly stable lead-free perovskite $Cs_3Sb_2Br_9$ quantum dots. *ACS Energy Lett.* **2020**, *5*, 385–394.
[48] Shao, W. Y.; Wang, X.; Zhang, Z. Z.; Huang, J.; Han, Z. Y.; Pi, S.; Xu, Q.; Zhang, X. D.; Xia, X. C.; Liang, H. W. Highly efficient and flexible scintillation screen based on manganese(II) activated 2D perovskite for planar and nonplanar high-resolution X-ray imaging. *Adv. Opt. Mater.* **2022**, *10*, 2102282.
[49] Wu, H. D.; Wang, Q.; Zhang, A.; Niu, G. D.; Nikl, M.; Ming, C.; Zhu, J. S.; Zhou, Z. Y.; Sun, Y. Y.; Nan, G. et al. One-dimensional scintillator film with benign grain boundaries for high-resolution and fast X-ray imaging. *Sci. Adv.* **2023**, *9*, eadh1789.
[50] Howansky, A.; Mishchenko, A.; Lubinsky, A. R.; Zhao, W. Comparison of CsI: Tl and Gd_2O_2S: Tb indirect flat panel detector X-ray imaging performance in front- and back-irradiation geometries. *Med. Phys.* **2019**, *46*, 4857–4868.

This is an open access article under the terms of the Creative Commons Attribution 4.0 International License (CC BY 4.0, https://creativecommons.org/licenses/by/4.0/).

© The Author(s) 2026. Published by Tsinghua University Press.